INTERNATIONAL JOURNAL FOR NUMERICAL METHODS IN FLUIDS
Int. J. Numer. Meth. Fluids 2009; **59**:535–557
Published online 19 June 2008 in Wiley InterScience (www.interscience.wiley.com). DOI: 10.1002/fld.1831

Boundary discretization for high-order discontinuous Galerkin computations of tidal flows around shallow water islands

P.-E. Bernard*,†, J.-F. Remacle and V. Legat

Institute of Mechanical, Materials and Civil Engineering, Université catholique de Louvain, Avenue Georges Lemaître 4, 1348 Louvain-la-Neuve, Belgium

SUMMARY

In this paper some preliminary results concerning the application of the high-order discontinuous Galerkin (DG) method for the resolution of realistic problems of tidal flows around shallow water islands are presented. In particular, tidal flows are computed around the Rattray island located in the Great Barrier Reef. This island is a standard benchmark problem well documented in the literature providing useful *in situ* measurements for validation of the model. Realistic elements of the simulation are a tidal flow forcing, a variable bathymetry and a non-trivial coastline.

The computation of tidal flows in shallow water around an island is very similar to the simulation of the Euler equations around bluff bodies in quasi-steady flows. The main difference lies in the high irregularity of islands' shapes and in the fact that, in the framework of large-scale ocean models, the number of elements to represent an island is drastically limited compared with classical engineering computations. We observe that the high-order DG method applied to shallow water flows around bluff bodies with poor linear boundary representations produces oscillations and spurious eddies. Surprisingly those eddies may have the right size and intensity but may be generated by numerical diffusion and are not always mathematically relevant. Although not interested in solving accurately the boundary layers of an island, we show that a high-order boundary representation is mandatory to avoid non-physical eddies and spurious oscillations. It is then possible to parametrize accurately the subgrid-scale processes to introduce the correct amount of diffusion in the model. The DG results around the Rattray island are eventually compared with current measurements and reveal good agreement. Copyright © 2008 John Wiley & Sons, Ltd.

Received 16 August 2007; Revised 26 March 2008; Accepted 27 March 2008

KEY WORDS: high-order discontinuous Galerkin method; shallow water equations; geophysical flows; boundary discretization; Rattray island

*Correspondence to: P.-E. Bernard, Institute of Mechanical, Materials and Civil Engineering, Université catholique de Louvain, Avenue Georges Lemaître 4, 1348 Louvain-la-Neuve, Belgium.
†E-mail: paul-emile.bernard@uclouvain.be

Contract/grant sponsor: Fonds pour la formation à la Recherche dans l'Industrie et dans l'Agriculture (FRIA, Belgium)
Contract/grant sponsor: Actions de Recherche Concertées; contract/grant number: ARC 04/09-316

1. INTRODUCTION

Most of the ocean models in use since 40 years are inspired by the work of Bryan [1]: the underlying discretization is based on finite difference schemes on structured grids. The use of unstructured meshes offers many advantages and is now commonly used in many fields of engineering applications. The development of such an ocean model based on unstructured grids does not consist in a simple extension of structured grid models but requires to rethink a complete model from the start. Unstructured meshes allow an accurate representation of complex geometrical features such as bathymetries or coastlines. They allow one to increase the resolution in regions of large gradients as the coasts, shelf breaks, polar fronts or transient processes as the Gulf Stream.

Several unstructured grid ocean models are under study since a decade using the finite element method [2–6], finite volumes [7, 8] or spectral elements [9]. The discontinuous Galerkin (DG) finite element method is a new trend for solving engineering problems where advection plays an important role [10–13]. It is now under study for ocean applications [14–17]. The DG method combines the advantaging features of both continuous finite elements and finite volumes. High-order polynomial function spaces are used to increase the resolution within elements without enlarging the stencils, while discontinuities allow one to build high-resolution advection schemes. The DG method also provides a simple and efficient way to perform h- and p-adaptivity [18, 19] and exhibits very interesting properties as a superconvergent behaviour for dissipation and dispersion errors [20–22], which is particularly interesting in many ocean processes. Yet the application of high-order DG method to realistic processes of ocean modelling is still a challenging issue, especially because of the complexity of the geometrical features as coastlines or bathymetry.

Section 2 presents the governing equations and their classical DG discretization including the derivation of the weak formulation and the flux computation with Riemann-like solvers. The following section deals with the issue of the boundaries discretization in the context of quasi-steady flows at low Froude numbers. Bassi and Rebay [23] have shown that a poor representation of the boundaries with piecewise linear edges does not lead to a steady-state solution for the benchmark of a cylinder in a mean flow using the Euler equations. The high-order DG method produces oscillations and spurious eddies in the wake of smooth bluff bodies with steady flow computations. We observe the same behaviour with the shallow water equations. A converged solution is obtained only with a more accurate boundary representation as a high-order mapping between the reference element and the real one or with techniques as the smoothing of the normals as proposed by Krivodonova and Berger [24]. However, in the presence of thousands of islands and coasts, we are restricted to the use of coarse meshes, which means a relatively low mesh resolution close to the boundaries. With too coarse meshes and especially irregular bluff bodies as islands, we observe that spurious oscillations are still generated with the reconstruction of a continuous linear representation of the normals, while the use of high-order mappings still avoids oscillations. Moreover, the continuous linear normals do not allow an accurate representation of the shape of boundaries for very irregular bluff bodies.

Finally, the last results deal with the computation of tidal flows around the Rattray island located in the Great Barrier Reef. The study of a hydrodynamic model of the Great Barrier Reef is particularly interesting since the coastal processes in this region exhibit the same kind of range of scales than the world ocean in a smaller domain of computation [25]. The main large-scale forcing is the oceanic inflow of the East Australian Current coming from the Coral Sea. This current flows westward into the shelf region and splits into two branches, creating a northward and a southward flowing current [26]. Those large-scale long shore currents may be strongly deviated

DOI: 10.1002/fld

by the wind, the tides and the topography. Thousands of islands and reefs generate small-scale eddies and tidal jets [27]. It is mandatory to simulate all scales simultaneously since small- and large-scale processes experience strong interactions. Moreover, increasing the resolution in a small area allows one to study this area without the drawback of imposing arbitrary boundary conditions around it.

In this framework of a large hydrodynamic model or world ocean model, we wish to perform flow computations around shallow water islands with meshes as coarse as possible. The realistic test case of the Rattray island is particularly interesting because many *in situ* measurements of elevation, velocity, tidal forcings, topology and bathymetry are available to validate and calibrate the model. It is clear that we are not interested in solving the boundary layer of the island. All we expect is to reach the correct rate of vorticity and the correct dispersion relation for wave propagation.

2. DG DISCRETIZATION OF THE SHALLOW WATER EQUATIONS

In the general mathematical framework of the DG methods, we consider a system of conservation laws expressed in the *conservative* form:

$$\frac{\partial \mathbf{U}}{\partial t} + \nabla \cdot \mathbf{F}(\mathbf{U}) = \mathbf{S}(\mathbf{U}) + \nabla \cdot \mathbf{D}(\mathbf{U}) \tag{1}$$

where $\mathbf{U}$ is the vector of unknown fields, $\mathbf{F}$ is the convective flux matrix containing the pressure and transport terms, $\mathbf{S}$ is the vector containing the so-called source terms that do not involve any derivative of the unknown fields and $\mathbf{D}$ is the diffusive flux matrix.

The domain of computation Ω is divided into a set of $\mathcal{N}_e$ non-overlapping elements Ω_e:

$$\Omega = \bigcup_{e=1}^{\mathcal{N}_e} \Omega_e$$

The standard DG weak formulation is obtained by multiplying Equation (1) by a smooth function $\hat{\mathbf{U}}$ and integrating on each element Ω_e:

$$\frac{\partial}{\partial t}\int_{\Omega_e} \mathbf{U}\hat{\mathbf{U}}\,\mathrm{d}\Omega_e + \int_{\Omega_e} \nabla \cdot \mathbf{F}(\mathbf{U})\hat{\mathbf{U}}\,\mathrm{d}\Omega_e = \int_{\Omega_e} \mathbf{S}(\mathbf{U})\hat{\mathbf{U}}\,\mathrm{d}\Omega_e + \int_{\Omega_e} \nabla \cdot \mathbf{D}(\mathbf{U})\hat{\mathbf{U}}\,\mathrm{d}\Omega_e \tag{2}$$

We seek an approximation $\mathbf{U}^h$ of $\mathbf{U}$ such that $\mathbf{U}^h \in \mathscr{U}_p^h$ with $\mathscr{U}_p^h$ the finite dimensional space composed of polynomial functions of order at most p on Ω_e. We define on each element a discrete representation $\mathbf{U}^h$ of $\mathbf{U}$ as

$$\mathbf{U}^h = \sum_{i=1}^{\mathcal{N}_\mathrm{d}} \phi_i \mathbf{U}_i \in \mathscr{U}_p^h$$

where $\mathbf{U}_i$ are the nodal values, ϕ_i are a set of independent shape functions and $\mathcal{N}_\mathrm{d}$ is the number of degrees of freedom on one element. Although there are many possible choices for the shape functions, we will consider Lagrange shape functions in the following developments. Therefore, the number of degrees of freedom on each element is related to the polynomial order p by the

DOI: 10.1002/fld

relation $\mathcal{N}_{\mathrm{d}}=(p+1)(p+2)/2$. The weak formulation is then discretized as

$$\frac{\partial}{\partial t}\int_{\Omega_e}\mathbf{U}^h\hat{\mathbf{U}}^h\,\mathrm{d}\Omega_e+\int_{\Omega_e}\nabla\cdot\mathbf{F}(\mathbf{U}^h)\hat{\mathbf{U}}^h\,\mathrm{d}\Omega_e=\int_{\Omega_e}\mathbf{S}(\mathbf{U}^h)\hat{\mathbf{U}}^h\,\mathrm{d}\Omega_e+\int_{\Omega_e}\nabla\cdot\mathbf{D}(\mathbf{U}^h)\hat{\mathbf{U}}^h\,\mathrm{d}\Omega_e \tag{3}$$

with the test function $\hat{\mathbf{U}}^h\in\mathscr{W}_p^h$.

Two neighbouring elements in continuous finite element method share common nodes that ensure the continuity of the finite element approximation and that allows an information transfer between elements. It is mandatory to ensure the same coupling between elements with the DG method, by the following integration by parts on the convective and diffusive terms:

$$\begin{aligned}&\frac{\partial}{\partial t}\int_{\Omega_e}\mathbf{U}^h\hat{\mathbf{U}}^h\,\mathrm{d}\Omega_e-\int_{\Omega_e}\mathbf{F}(\mathbf{U}^h)\cdot\nabla\hat{\mathbf{U}}^h\,\mathrm{d}\Omega_e+\int_{\partial\Omega_e}\mathbf{F}(\mathbf{U}^h)\cdot\mathbf{n}\hat{\mathbf{U}}^h\,\mathrm{d}\Gamma_e\\&\quad=\int_{\Omega_e}\mathbf{S}(\mathbf{U}^h)\hat{\mathbf{U}}^h\,\mathrm{d}\Omega_e-\int_{\Omega_e}\mathbf{D}(\mathbf{U}^h)\cdot\nabla\hat{\mathbf{U}}^h\,\mathrm{d}\Omega_e+\int_{\partial\Omega_e}\mathbf{D}(\mathbf{U}^h)\cdot\mathbf{n}\hat{\mathbf{U}}^h\,\mathrm{d}\Gamma_e\end{aligned} \tag{4}$$

where $\mathbf{n}$ denotes the outgoing unit normal to element Ω_e, and Γ_e denote the edges of this element.

The main difference with the continuous finite element method lies in the fact that the discrete solution presents different values, say $\mathbf{U}_{\mathrm{L}}$ and $\mathbf{U}_{\mathrm{R}}$, at the discontinuity between elements. Formulation (4) is thus somehow ambiguous and incomplete since the discretization leads to a discrete normal flux function $\mathbf{F}(\mathbf{U}^h)\cdot\mathbf{n}$ depending on both right and left values at the discontinuity:

$$\mathbf{F}(\mathbf{U}^h)\cdot\mathbf{n}=\mathbf{F}(\mathbf{U}_{\mathrm{L}},\mathbf{U}_{\mathrm{R}})\cdot\mathbf{n} \tag{5}$$

This flux function has to be properly defined since it will be responsible in a large part for the accuracy and robustness of the scheme. This discontinuity provides a way of introducing accurate advection schemes, which makes the DG method very efficient for advection-dominated processes. The flux computation is based on the idea of the Riemann solver and the characteristics theory: the hyperbolic system of equations is decomposed into a set uncoupled scalar advection equations, advecting the Riemann invariants along characteristic curves. The flux function used in this study is based on the simple Lax–Friedrich flux $\mathbf{F}^{\mathrm{LF}}$:

$$\mathbf{F}^{\mathrm{LF}}(\mathbf{U})=0.5(\mathbf{F}(\mathbf{U}_{\mathrm{L}})+\mathbf{F}(\mathbf{U}_{\mathrm{R}}))+0.5|\lambda|_{\max}(\mathbf{U}_{\mathrm{L}}-\mathbf{U}_{\mathrm{R}}) \tag{6}$$

where $|\lambda|_{\max}$ denotes the maximum absolute value of the eigenvalues of the system, i.e. the propagation speed of the information. Other more complex Riemann-like solvers can be used as, for instance, a Godunov solver or a Roe solver [28–31], whose expression for the shallow water equations may be found in [19, 32]. However, the results obtained for the shallow water equations do not present significant differences for any of those fluxes.

The discontinuities between elements also lead to many different ways of treating the diffusive flux [33]. Indeed, the solution gradients are not well defined at the discontinuities, as the solution itself. In this study we consider the classical *local discontinuous Galerkin* (LDG) method proposed by Bassi and Rebay [34, 35]. This technique consists basically in computing the solution gradients at the interfaces as a function of the gradients on both surrounding elements and of the jumps of the solution. This method is well suited for explicit time schemes as we consider in this paper. However, other techniques for computing diffusion operators will be considered in future works for handling implicit time schemes more easily, as the *interior penalty* methods [36, 37].

DOI: 10.1002/fld

2.1. Application to the shallow water equations

The set of the shallow water equations represents the flow of a thin layer of incompressible fluid under the influence of a gravitational force in a rotating framework. Those equations can be obtained from the vertical integration of the incompressible 3D Navier–Stokes equations with impermeability boundary conditions on the surface and bottom of the ocean [38, 39].

Let us first express the conservation equations in the generic form (1). The mass conservation equation of the shallow water model reads

$$\frac{\partial \eta}{\partial t} + \nabla \cdot (H\mathbf{v}) = 0 \tag{7}$$

where $\mathbf{v} = (u, v)$ and η are the mean horizontal velocity and the sea surface elevation, respectively, $H = h + \eta$ is the water elevation and h is the bathymetry, water depth below the mean sea level, as illustrated in Figure 1. The momentum conservation equation reads

$$\frac{\partial H\mathbf{v}}{\partial t} + \nabla \cdot (H\mathbf{v}\mathbf{v}) + gH\nabla\eta + f\mathbf{e}_z \times H\mathbf{v} = \boldsymbol{\tau}^s - \gamma\mathbf{v}\|\mathbf{v}\| + \nu\nabla \cdot (H\nabla\mathbf{v}) \tag{8}$$

where the Coriolis parameter, the acceleration due to the gravity, the mean water density and the horizontal eddy viscosity are denoted by f, g, ρ and ν, respectively. Vector $\mathbf{e}_z$ denotes the local normal unit vector to the geopotential surface. The diffusion term does not represent the viscous terms of the Navier–Stokes equations, which are neglected, but represents the subgrid-scale processes. It is then mandatory to modelize the subgrid-scale viscosity ν as a function of the element size, especially in multi-scale computations as finite element ocean modelling. At the bottom, the friction is parametrized with a quadratic relationship where $\|\mathbf{v}\|$ is the amplitude of the velocity and γ is a friction coefficient. At the sea surface, the wind stress is given by $\boldsymbol{\tau}^s = (\tau_x, \tau_y)$. Both Equations (7) and (8) can be injected in the generic form (1), by defining $\mathbf{U}$, $\mathbf{S}$, $\mathbf{D}$ and $\mathbf{F}$ as follows:

$$\mathbf{U} = \begin{bmatrix} \eta \\ Hu \\ Hv \end{bmatrix}, \quad \mathbf{F}(\mathbf{U}) = \begin{bmatrix} Hu & Hv \\ Huu + g\dfrac{H^2 - h^2}{2} & Huv \\ Hvu & Hvv + g\dfrac{H^2 - h^2}{2} \end{bmatrix}$$

$$\mathbf{S}(\mathbf{U}) = \begin{bmatrix} 0 \\ g\eta\partial_x h + fHv + \tau_x^s - \gamma u\|\mathbf{v}\| \\ g\eta\partial_y h - fHu + \tau_y^s - \gamma v\|\mathbf{v}\| \end{bmatrix}, \quad \mathbf{D}(\mathbf{U}) = \begin{bmatrix} 0 & 0 \\ \nu H\partial_x u & \nu\partial_y u \\ \nu H\partial_x v & \nu\partial_y v \end{bmatrix} \tag{9}$$

Large-scale ocean processes as basin gyres or anticyclonic eddies are usually dominated by the geostrophic balance, i.e. the balance between the pressure term and the Coriolis term. The aim is to compute the perturbations of this equilibrium as the Rossby waves or the advection terms, but the pressure term $gH\nabla\eta$ is the dominating term in the system for that kind of processes. To express it as flux with a divergence form, we observe that it must be expressed as $g\nabla(H^2 - h^2) - g\eta\nabla h$. With a non-constant bathymetry, the dominating term of the system is thus split into two parts: one computed through the fluxes with an approximate Riemann solver and the other one considered

DOI: 10.1002/fld

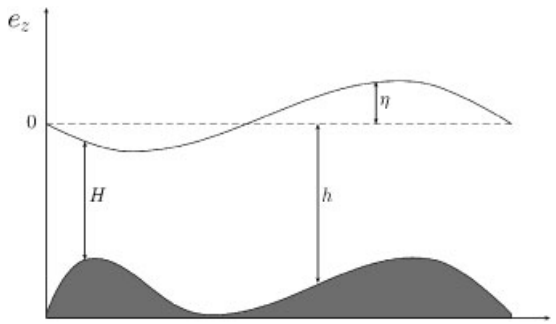

Figure 1. Shallow water configuration for water depth H with a time-independent bathymetry h and a relative elevation η, usually several orders of magnitude lower than the bathymetry.

as a *source* term. It is then mandatory to integrate accurately those two terms to avoid spurious gravity waves. Indeed, strong oscillations and spurious waves may be observed, especially with a strongly varying bathymetry, when using quadrature-free techniques or very distorted curved elements, which may involve lack of accuracy in the integration process.

We must finally note at this point that, depending on the application, it could be useful to consider an alternative formulation of the momentum equation, obtained by substituting (7) into (8) and dividing by H:

$$\frac{\partial \mathbf{v}}{\partial t}+\mathbf{v}\cdot\nabla\mathbf{v}+g\nabla\eta+f\,\mathbf{e}_z\times\mathbf{v}=\frac{\boldsymbol{\tau}^s}{H}-\gamma\frac{\mathbf{v}}{H}\|\mathbf{v}\|+\frac{\nu}{H}\nabla\cdot(H\nabla\mathbf{v}) \tag{10}$$

Although both formulations are strictly equivalent in the continuous world, their discretizations may lead to quite a different discrete algebraic system. Indeed, the advection terms have to be split into two terms to be expressed in the divergence form, while the pressure term $g\nabla\eta$ is no more splitted. Therefore, where the pressure term appears to be the main driving term, this second formulation could appear to be more robust and accurate since a lack of accuracy in the integration will not generate spurious waves as in the first formulation.

3. COMPUTATION OF SHALLOW WATER FLOWS AROUND OBSTACLES

It is well known that the discontinuous Galerkin method is very accurate and efficient for computing advection-dominated processes because of, for instance, the simple use of high-order elements with accurate advection schemes, the very efficient error estimation in the inter-element jumps, or the highly parallelizable nature of the method. In particular, the DG method becomes very efficient when using high-order function space. Indeed, it exhibits superconvergence properties for the dispersion and dissipation errors, $\mathcal{O}(h^{2p+3})$ and $\mathcal{O}(h^{2p+2})$, respectively, and for the discretization errors with a convergence rate of $\mathcal{O}(h^{p+1})$. The purpose of the present study in thus to investigate the use of *high-order* polynomial orders for computing shallow water flows on *coarse meshes* in the context of ocean modelling in order to benefit from those convergence properties.

A first simple benchmark consists in a cylinder in a constant mean flow. Without the diffusion process, we should observe the convergence to a well-known steady solution, as for the Euler equations. The second more realistic benchmark of the Rattray island will then be investigated and

DOI: 10.1002/fld

the results will be compared with *in-situ* measurements. The following computations have been performed using an explicit classical Runge–Kutta time scheme.

3.1. Cylinder test case

Let us consider a cylinder in a mean flow with a Froude number of $Fr=0.2$. This non-dimensional number is similar to the Mach number in the Euler equations and is defined as the ratio of the fluid velocity to the gravity wave speed. The source terms and dissipation processes are not considered, which implies no diffusion term, no Coriolis force, no bathymetry gradient and no bottom or surface stress. We use a bathymetry of 1 m, which corresponds for a gravitational acceleration of $g=9.81\,\mathrm{m\,s^{-2}}$ to the imposition of a zero elevation and a constant velocity of $0.2\sqrt{9.81}\cong 0.63\,\mathrm{m\,s^{-1}}$ on the boundaries. A slip boundary condition on the cylinder is also mandatory to obtain a steady converged solution.

With the use of the DG method and a piecewise linear representation of the cylinder boundary, the solution does not reach the expected steady state unless a special treatment of the boundaries is applied, as shown by Bassi and Rebay for the 2D Euler equations [23]. Oscillations appear in the vicinity of the obstacle. They grow and propagate in constant or quasi-constant mean flows as tidal flows, leading to the creation of vorticity and of a wake behind the bluff body. Those oscillations are enforced when using higher polynomial orders. This issue is illustrated in the left part of Figure 2: strong oscillations are observed with second-order Lagrange shape functions and a piecewise linear representation of the boundaries, generating non-physical eddies in the wake of the cylinder and polluting the solution far away from the boundaries.

Many techniques allow one to obtain the expected solution. A very cheap and efficient technique proposed by Krivodonova and Berger [24] consists in building a continuous representation of the normals and in using those smooth normals in the Riemann solver computation, while keeping the discontinuous representation in the integration on the edges. This continuous representation is depicted in the left column of Figure 3. This technique yields the expected steady solution as depicted in the right part of Figure 2.

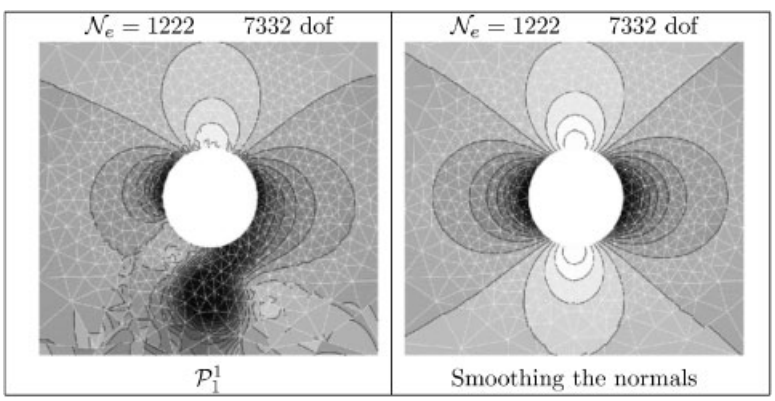

Figure 2. Water elevation field for a mean flow around a cylinder with second-order Lagrange shape functions and a Froude number of $Fr=0.2$. Oscillations appear with a classical piecewise linear representation of the boundaries (left) and prevent convergence to the steady solution. The smoothing of the normals proposed by Krivodonova and Berger suppresses those oscillations and leads to the converged solution (right).

DOI: 10.1002/fld

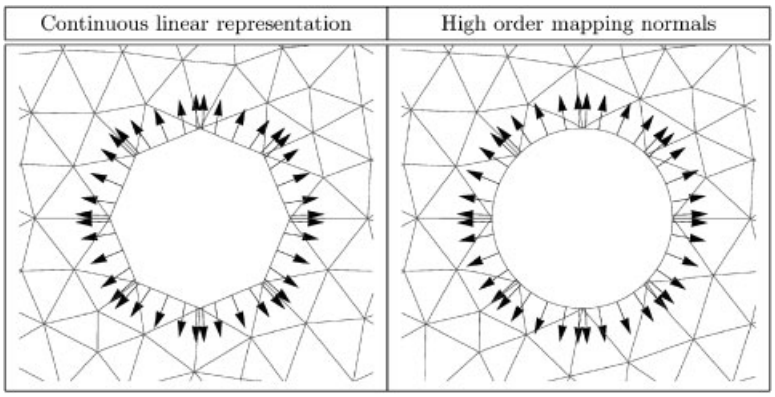

Figure 3. The continuous representation of the normals according to Krivodonova and Berger (left) is quite similar to the normals computed from a high-order mapping of the triangles (right).

However, the drawback of this technique lies in the reduction in the convergence rates when using sufficiently high-order shape functions. Moreover, although this technique works perfectly for sufficiently refined meshes and smooth bluff bodies, oscillations may rapidly appear when using very irregular bluff bodies. Finally, the linear reconstruction of the normals does not represent accurately very irregular obstacles, as depicted in the left part of Figure 4.

Another approach used in this study consists in building high-order meshes, i.e. using curved triangles with high-order polynomial mappings, to obtain a better representation of irregular bluff bodies. We consider a triangle composed of a set of $\mathcal{N}_c$ coordinates $\mathbf{X}$. A possible continuous representation $\mathbf{x} \in \mathscr{R}^2$ of the triangle is given by the simple polynomial mapping

$$\mathbf{x}_j = \sum_{i=1}^{\mathcal{N}_c} \psi_i(\boldsymbol{\xi}) \mathbf{X}_{i,j}, \quad j = 1, 2 \text{ in 2D} \tag{11}$$

where $\psi(\boldsymbol{\xi})$ denotes the shape functions corresponding to the coordinates $\mathbf{X}$ in the bi-dimensional parametric space $\boldsymbol{\xi} = (\xi, \eta)$.

A possible representation consists in using Lagrange shape functions as for the polynomial representation of the solution. A mapping of order q is then obtained for a number of coordinates $\mathcal{N}_c$ such that

$$\mathcal{N}_c = \frac{(q+1)(q+2)}{2}$$

However, the high-order Lagrange shape functions present nodes located inside the triangle. The position of those nodes is somehow arbitrary and does not bring more information on the boundary representation, while the nodes' coordinates on the edges are computed, for instance, as equidistant on the parametric curve representing the boundary. We thus use in this study Serendip shape functions, i.e. incomplete shape functions at order q, with nodes located only on the edges of the elements. We thus specify for a q-order *Serendip mapping* a number of coordinates:

$$\mathcal{N}_c = 3q$$

DOI: 10.1002/fld

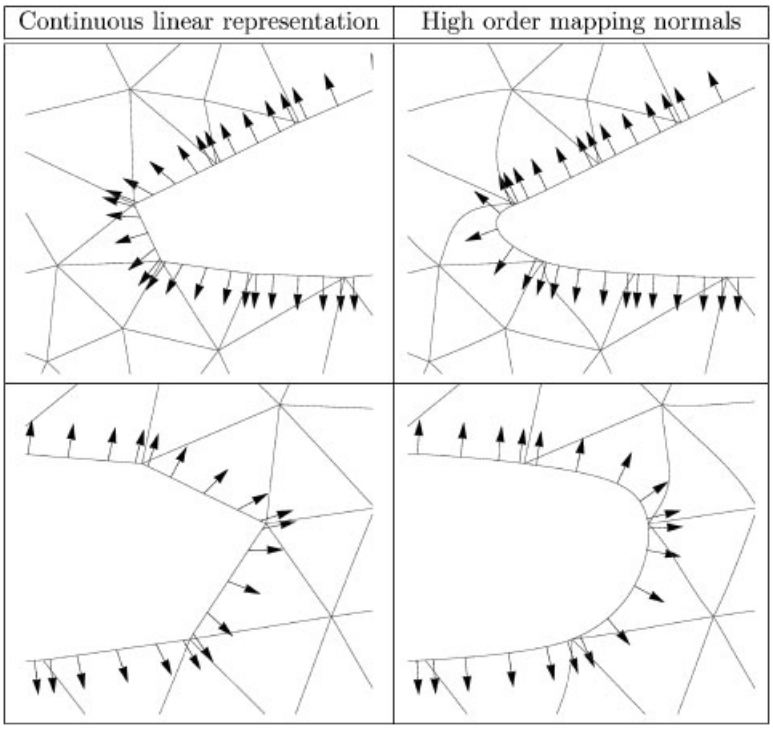

Figure 4. Different normals representations on the west (upper row) and east (bottom row) parts of the Rattray island. The continuous representation of the normals (left) becomes quite different from the normals computed from a high-order mapping of the triangles (right) for very irregular bluff bodies.

Let us introduce the following notation $\mathscr{P}_p^q$, denoting a p-order representation of the solution, using the Lagrange shape function, and a q-order incomplete Serendip mapping for the representation of the curved mesh.

Considering smooth bluff bodies as the cylinder, the continuous linear representation of the normals as proposed by Krivodonova and Berger is quite similar to the normals based on a high-order polynomial mapping, as depicted in Figure 3 where a third-order mapping is used. However, the difference becomes significative on very irregular boundaries and coarse meshes as depicted in Figure 4. For this kind of irregular bluff bodies, the use of high-order mappings provides a better representation of the boundaries and seems to reduce the generation of the spurious oscillations. One can observe in Figure 4 that the mesh has been optimized to decrease the elements' distortion: not only the elements that have a common edge with the domain boundaries are curved. Indeed, it is often necessary to curve some internal edges in order to maintain a valid mesh [40]. The high-order curved meshes used in this study have been generated by the mesh generator GMSH freely available at http://geuz.org/gmsh/ and described in [41].

The results obtained with high-order mappings are depicted in Figure 5. We observe the influence of both the mesh resolution and the polynomial order with third-order mappings. We consider two different meshes (white triangles) of 674 (upper row) and 245 (lower row) elements. The first computation on the finer mesh (left part of the figure) uses a second-order polynomial representation

DOI: 10.1002/fld

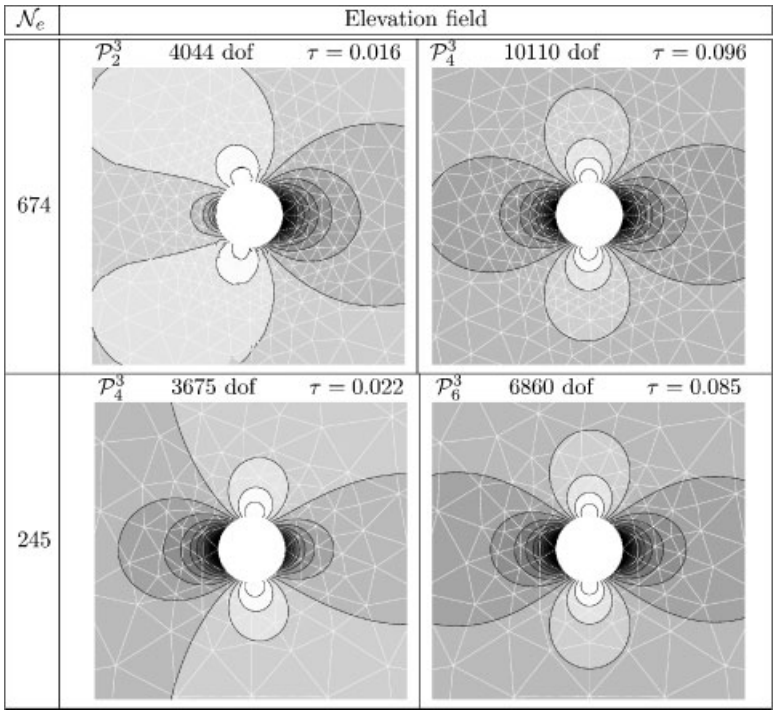

Figure 5. Water elevation fields for a mean flow around a cylinder with third-order mapping meshes of 674 (upper row) and 245 (lower row) elements. Obtaining the converged steady solution on the coarser grid requires a polynomial order up to order 6, while the order 4 is sufficient on the finer mesh. Only eight triangles are sufficient to accurately represent the boundaries with a third-order mapping. The relative computational times τ have been normalized with the maximum computation time obtained for the $\mathscr{P}_1^1$ representation in Figure 6.

of the solution, $\mathscr{P}_2^3$. This representation produces a relatively smooth solution, but the expected converged solution is not obtained because of the high sensitivity of the method to the asymmetry of the mesh. The pressure becomes higher on the right-hand side of the cylinder, leading to an oscillating solution with non-symmetric stagnation points. One can thus increase the polynomial order or the mesh resolution. The fourth-order representation, $\mathscr{P}_4^3$, on the same mesh, leads to the expected solution. Decreasing the mesh resolution (bottom row of the figure), the polynomial order has then to be increased up to order 6 to obtain the converged solution.

We observe that only eight triangles are sufficient with a third-order mapping to accurately represent the cylinder boundaries. However, the convergence of the solution to the exact steady state also requires a sufficient resolution, which can be reached by a sufficiently high polynomial order and/or a sufficiently high mesh resolution. We also observe in Figure 6 that the mesh resolution does not replace the accurate representation of the boundaries: the solution is obtained with a very fine grid of 20 016 triangles and a $\mathscr{P}_1^1$ representation, for which the converged solution is not reached. The solution clearly presents strong oscillations in the vicinity of the cylinder and the amplitude of the jumps in the wake of the bluff body suggests a high error compared with the high-order mappings solutions. The comparison between the high-order $\mathscr{P}_6^3$ and the linear $\mathscr{P}_1^1$

DOI: 10.1002/fld

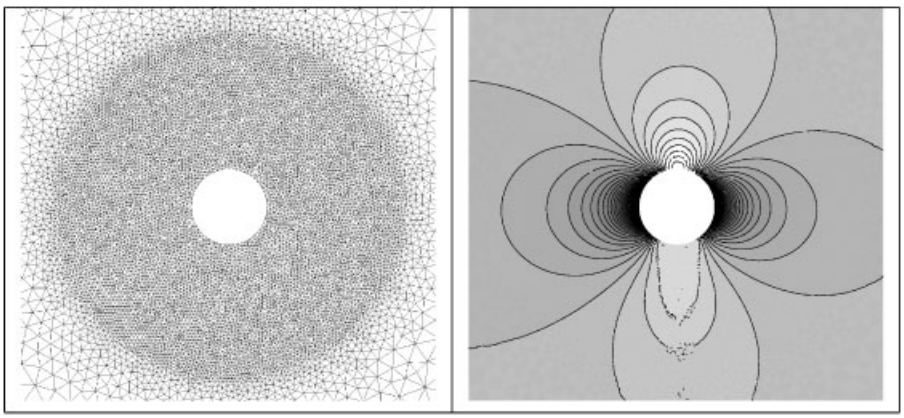

Figure 6. Elevation field (right) computed on the fine mesh (left) with a $\mathscr{P}_1^1$ representation. Although using a relatively fine mesh (20 016 elements), the poor representation of the boundaries generates strong oscillations on the boundaries and in the wake of the cylinder and does not allow the obtention of the expected converged solution.

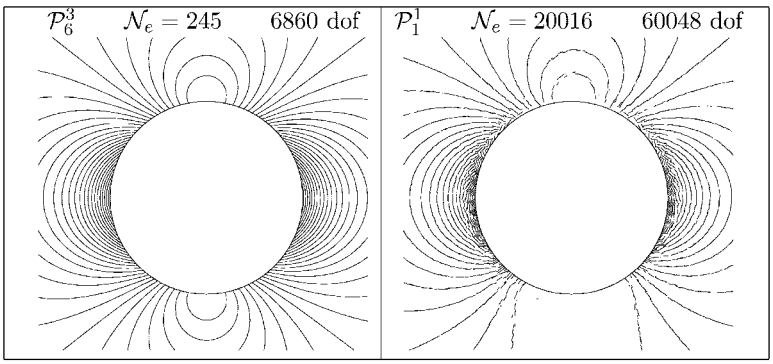

Figure 7. Close-up views of the cylinder vicinity for comparison of the solutions obtained with the $\mathscr{P}_6^3$ representation on the 245 elements mesh (left) and a $\mathscr{P}_1^1$ representation on a 20 016 elements mesh (right). The $\mathscr{P}_6^3$ computation presents about nine times less degrees of freedom for a more accurate solution.

representations is depicted in the close-up views of Figure 7. We observe that the solution is clearly more accurate with the $\mathscr{P}_6^3$ representation, which presents about nine times less degrees of freedom than the $\mathscr{P}_1^1$ representation. The relative computational costs τ of the different computations given in Figure 5 have been normalized with the maximum computational time, i.e. the one of the $\mathscr{P}_1^1$ computation. Considering that the converged steady solutions are reached only for the $\mathscr{P}_4^3$ and $\mathscr{P}_6^3$ representations with meshes of 674 and 245 elements, respectively, the lower computational time corresponds clearly to the use of the higher order, i.e. $p=6$, as expected.

Such curved meshes represent a powerful tool for handling *hp* adaptivity on complex geometries and boundaries [40]. However, the creation of curved meshes with really high-order mappings is sometimes quite difficult without generating jacobian matrices with negative determinants,

DOI: 10.1002/fld

or simply bad-shaped elements. Indeed, even if presenting strictly positive determinants of the jacobian matrix, very distorted elements cannot be used since the integration errors become very significative. Mesh generation procedures that adapt the element size and mapping order to the boundary curvature are essential tools for meshing really complex domains as the ocean with a low number of curved elements, but it is mandatory to keep the elements' distortion as low as possible.

We observe with this first test case that the DG method with the shallow water equations presents the same behaviour than with the Euler equations. With unstructured meshes around bluff bodies, an accurate representation of the boundaries and a sufficiently high resolution are mandatory to reach the expected converged solution and to avoid spurious eddies production when working with coarse meshes.

Techniques such as the smoothing of the normals are cheaper than the use of high-order mappings in terms of computational costs and are working perfectly well for flows around smooth bluff bodies. However, this method does not suppress oscillations for very irregular bluff bodies with sharp coasts and does not represent irregular boundaries in an accurate way, while the high-order mapping still produces smooth solutions.

3.2. Rattray island in a constant mean flow

The Rattray island is located at the coordinates 19°59′S, 148°33′E in the Great Barrier Reef near Australia. The island is 1.5 km long, 300 m wide and lies in well-mixed water. The surrounding bathymetry is approximately of 25 m but presents some strong varying gradients as depicted in Figure 12. This site has been chosen for many studies and measurements. Indeed, the surrounding waters are turbid, which allows aerial observations of the circulation and the scales are the typical coastal water scales [42].

This is thus a particularly interesting test case for numerical computations since it provides realistic and complex bathymetries and boundaries as shown in Figure 12, but also many measurements performed during several days, providing useful data for the tidal forcings (see Figure 11) and for comparison in the wake of the island.

The tides are almost perpendicular to the main island direction, creating eddies in its wake. Numerically speaking, those eddies are generated through the subgrid-scale processes, which means that a diffusion term has to be introduced and parametrized to reproduce those processes, with a larger diffusivity than the molecular diffusivity. The curl operator applied to the momentum equation yields an advection equation of the vorticity. In a constant mean flow with a flat bathymetry, no source term or diffusion term and slip boundary conditions, there should not be any vorticity generation inside the flow even in the presence of very irregular bluff bodies.

In the first numerical experiment we consider the Rattray island in a constant mean flow with a Froude number of $Fr = 0.1$ with a flat bathymetry of 25 m. No diffusion, Coriolis or bottom stress terms were considered while a slip boundary condition is imposed on the island's coast. The flow is then supposed to remain steady without vorticity production.

This experiment illustrates the issue of boundary discretization in ocean processes. The mesh of the idealized Rattray island depicted in Figure 8 is used with both $\mathscr{P}_4^1$ and $\mathscr{P}_4^2$ representations. Figure 9 shows the non-steady solution obtained with the first-order mapping: the linear discretization of the boundaries combined with a high-order DG scheme produces oscillations and numerical diffusion, responsible for the creation of non-physical eddies even with slip boundary conditions. Their size and amplitude depend on the boundary representation and on the elements size, which

DOI: 10.1002/fld

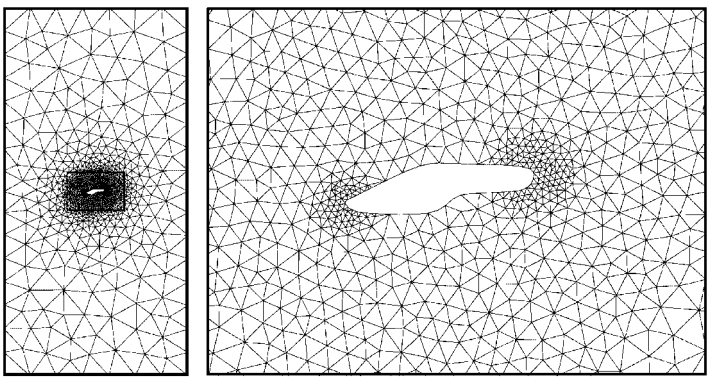

Figure 8. Mesh of the idealized Rattray island used for the Rattray experiments in a constant mean flow, with fourth-order polynomial function spaces and both first- and second-order mappings.

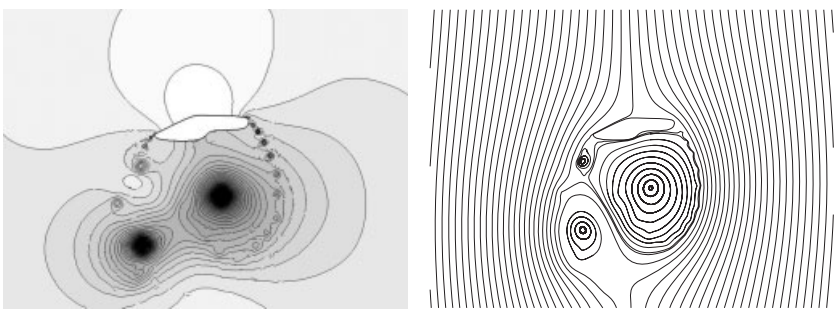

Elevation field Particles path

Figure 9. Without variable bathymetry, diffusion, Coriolis or bottom stress term, the expected steady-state solution in a constant mean flow is not obtained with a $\mathscr{P}_4^1$ representation. Spurious eddies are created on the poorly discretized boundaries; their size is the smallest element size.

means that we have no control on those spurious eddies. The smallest eddies ejected from the island edges merge in the wake of the island to create larger eddies. Those larger eddies always grow until they reach a length of the order of the island length. They finally reach the right sizes and amplitudes but not for the right reason. It can be shown that with a no slip boundary condition, the amount of vorticity expelled from the island coastlines does not depend on the boundary layer details, but depends only on the mean flow velocity, and the eddy size depends mainly on the length of the obstacle.

The second experiment in Figure 10 is obtained with exactly the same parameters, mesh and solution shape functions, but with a second-order mapping. The sufficiently accurate boundary representation leads to the expected steady solution without any spurious eddy. The DG scheme with appropriate boundary representation provides an advection scheme that does not require the use of numerical dissipation for its stabilization and avoid spurious oscillations. The vorticity and eddies generated then depend only on the subgrid-scale parametrization and can then be properly controlled.

DOI: 10.1002/fld

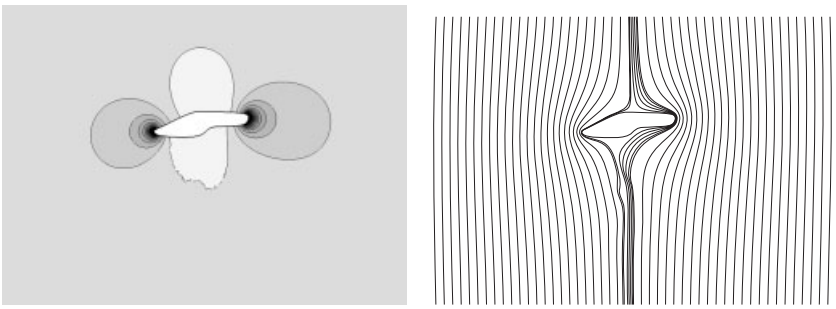

Elevation field Particles path

Figure 10. Steady-state solution for a constant mean flow with $Fr=0.1$ around the Rattray island without bathymetry, diffusion, Coriolis or bottom stress. Increasing the representation to $\mathscr{P}_4^2$ leads to a numerical scheme creating no eddies in the wake of the island.

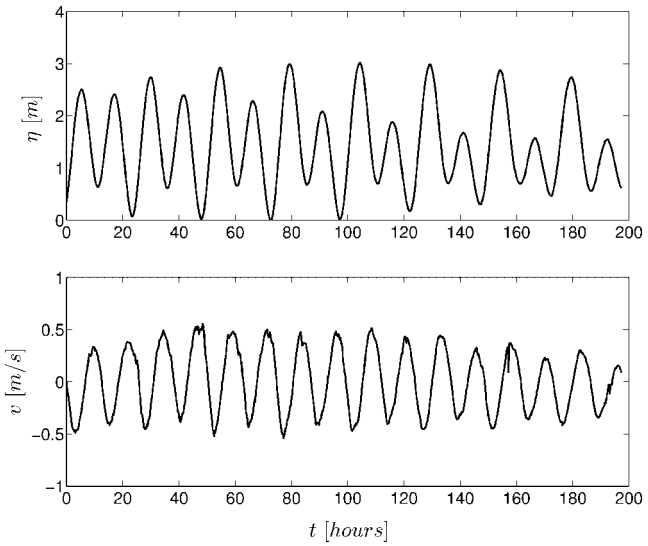

Figure 11. Time evolution of elevation and velocity (v-component) tide forcings measured in November 1982 near the Rattray island.

3.3. Realistic tidal flows around the Rattray island

The previous section has shown that the DG scheme with appropriate boundary conditions does not produce any spurious eddy and the numerical diffusion introduced by the scheme is not significative compared with the subgrid-scale viscosity. We may now introduce the horizontal diffusion terms to modelize those subgrid-scale processes. We use a variable viscosity as proposed by Smagorinsky [43] and White and Deleersnijder [6], depending on the element size and on the velocity field gradients:

$$\nu(x, y, t) = c\triangle(\mathbf{d}:\mathbf{d})^{1/2} \tag{12}$$

DOI: 10.1002/fld

where $\triangle$ denotes the element area and $\mathbf{d}$ is the infinitesimal deformation tensor defined as $\mathbf{d}=0.5(\nabla\mathbf{v}+\nabla\mathbf{v}^{\mathrm{T}})$. The parameter c is a constant, which has to be correctly chosen to obtain the right diffusivity and velocity amplitudes around the island. With this mesh and polynomial order, it is set to 0.1.

The physical parameters are $\rho=1000\,\mathrm{kg\,m^{-3}}$, $g=9.81\,\mathrm{m\,s^{-2}}$ and $\gamma=2\times10^{-3}$; the Coriolis parameter is approached with the f-plane approximation, $f=-5\times10^{-5}\,\mathrm{s^{-1}}$, corresponding to the latitude of 20°S and no wind forcing is considered. A second-order polynomial representation of the bathymetry is used with a restriction on the minimum bathymetry value set to 3 m to avoid any wetting/drying process.

Figure 13 shows the typical elevation and velocity fields obtained around the Rattray island with a curved coarse high-order mesh. Those results are in perfect agreement with the observations. The same computation with a piecewise linear representation of the boundaries produces spurious oscillations, which eventually lead to an unstable scheme. Indeed, with the use of the realistic bathymetry, the elevation oscillations become even larger than the water elevation itself. The use of an accurate representation of the boundaries is thus mandatory.

At the rising tide, a large clockwise rotating eddy is created on the southwest side of the island after about 1 h. It grows and reaches approximately twice the width of the island [44]. A second eddy is created in the western part of the island, but its size remains very small compared with the eastern eddy and compared with the first computation with a flat bathymetry. It is due to the very shallow bathymetry and the resulting high bottom stress. This smaller eddy that has not been observed *in situ* has been already reproduced by many numerical schemes and models [6, 45]. As the tide reverses, two counter-rotating eddies are generated on the northern side of the island. The maximum variable diffusivity is located on elements close to the island and reaches approximately $5\,\mathrm{m^2\,s^{-1}}$, which corresponds to the maximum velocities of about $1\,\mathrm{m\,s^{-1}}$ observed *in situ*.

Currentmeters depicted in Figure 12 were deployed on 23 November 1982, during almost 14 days. Good agreement of the v-component of the velocity through time is observed in Figure 15.

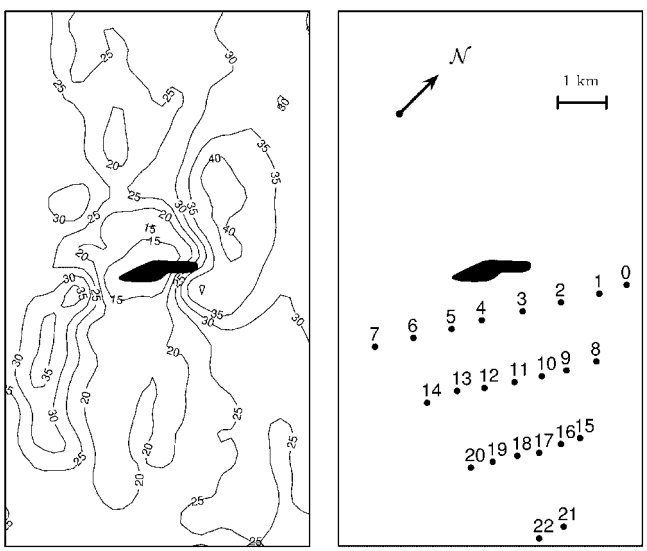

Figure 12. Bathymetry isolevels (left) and currentmeters position (right) around the Rattray island.

DOI: 10.1002/fld

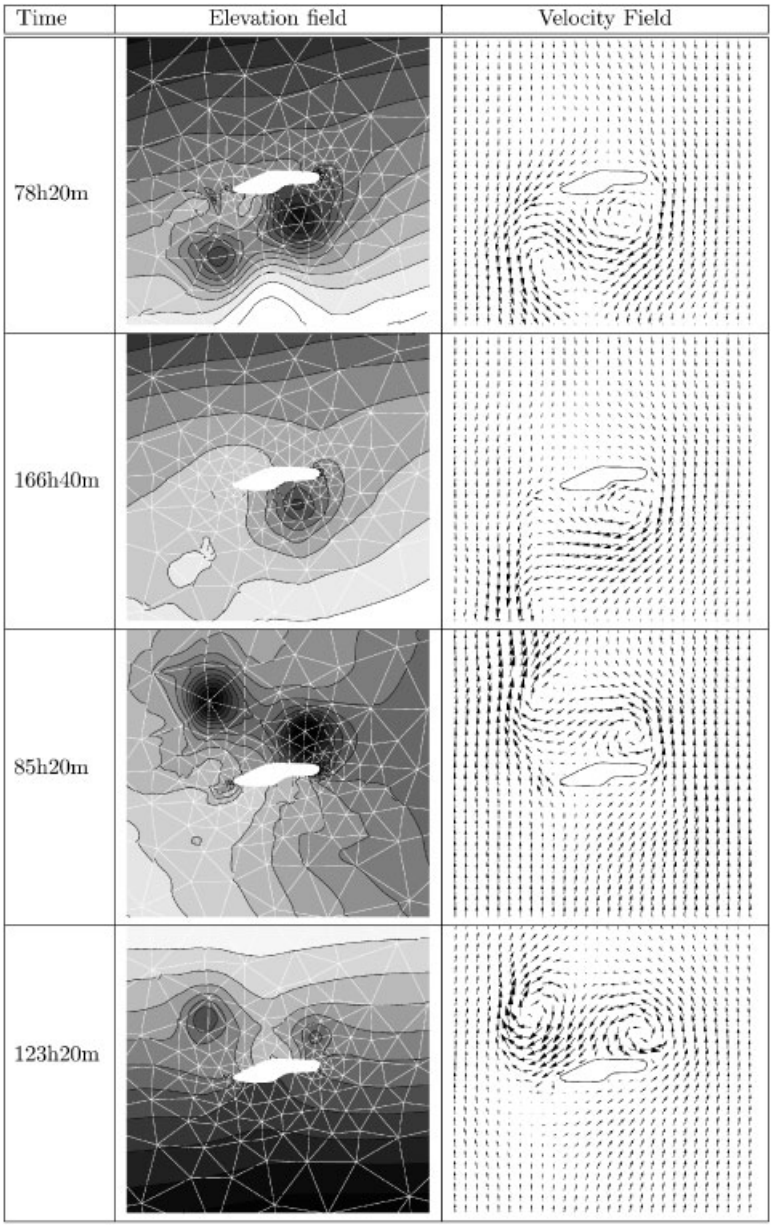

Figure 13. Typical elevation and velocity fields with tidal flows around the Rattray island on a coarse mesh using a $\mathscr{P}_4^3$ representation. The very shallow bathymetry on the southeast part of the island tends to reduce the size of the eastern eddy at rising tides (first two upper rows). The falling tide produces the two observed eddies on the northern side (bottom two rows).

DOI: 10.1002/fld

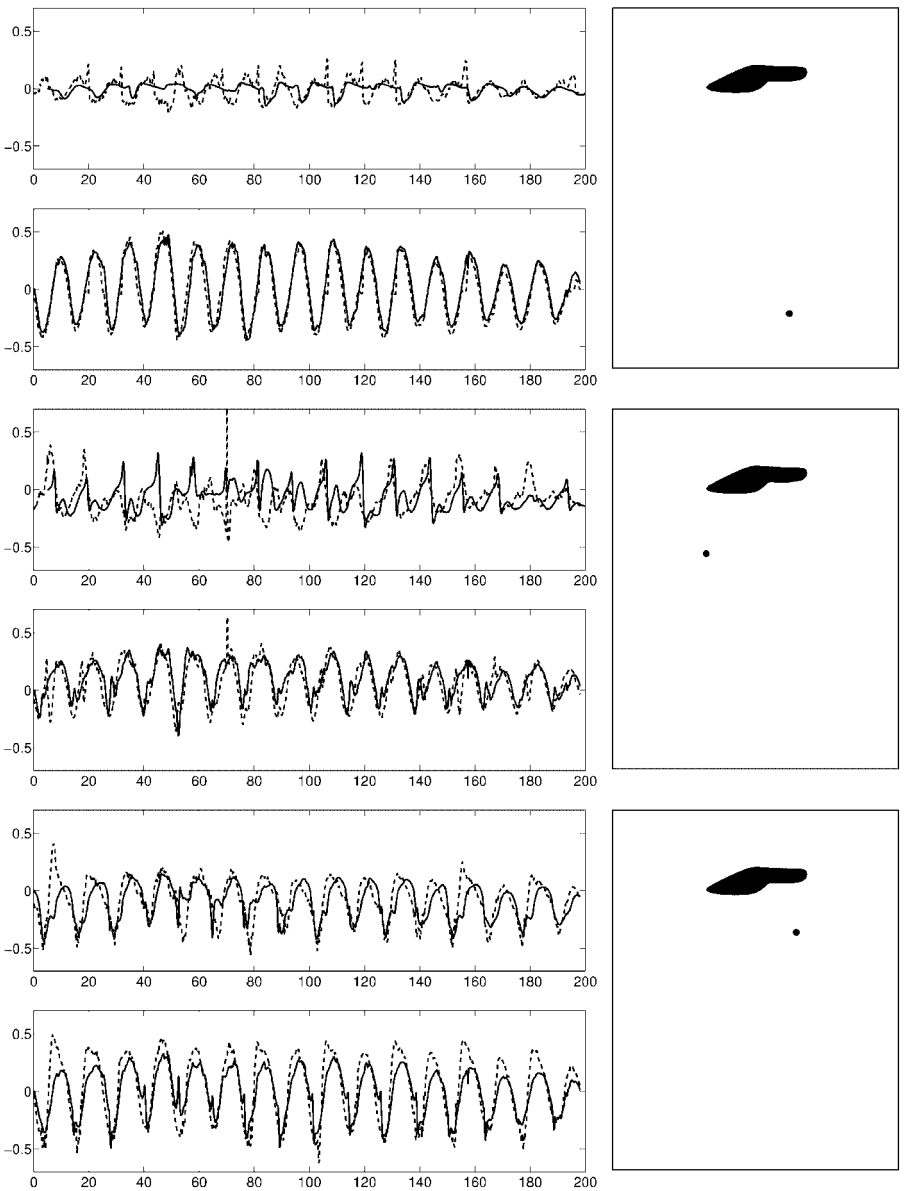

Figure 14. Comparison of the evolution in time (in hours) of the u- and v-components of the velocity (in $\mathrm{m\,s^{-1}}$) for some currentmeters. The DG results (continuous lines) and the measurements (dashed lines) are in good agreement for the v-component. The u-component is in better agreement for currentmeters close to the island, in the eddy region with larger amplitudes.

The evolution of the u-component, usually several orders of magnitude lower than v, does not fit as well the data since the numerical results are highly sensitive to topological differences with the real configuration. However, good agreement in velocity amplitude and time evolution for

DOI: 10.1002/fld

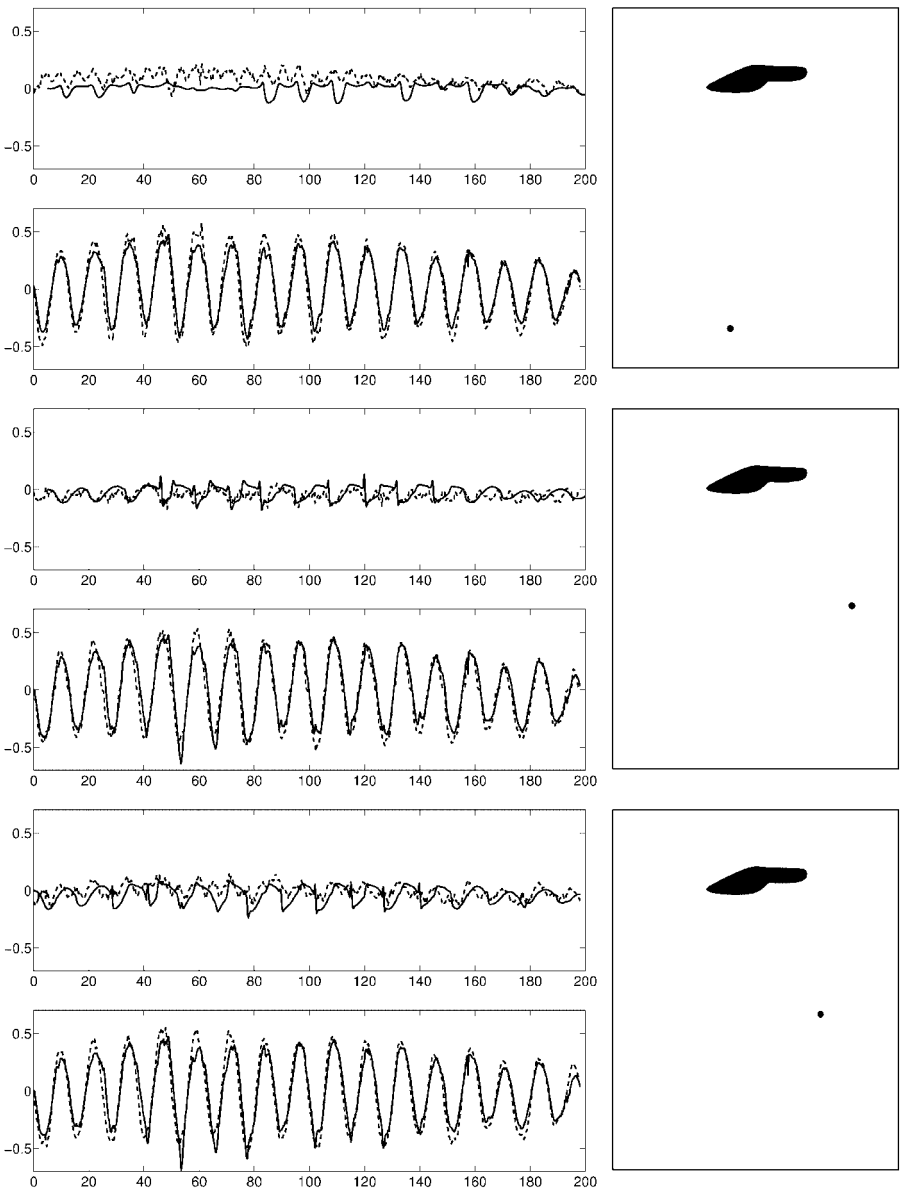

Figure 15. Comparison of the evolution in time (in hours) of the u and v-components of the velocity (in $\mathrm{m\,s^{-1}}$) for some currentmeters. The DG results (continuous lines) and the measurements (dashed lines) are in good agreement for the v-component. The u-component is in better agreement for currentmeters close to the island, in the eddy region with larger amplitudes.

DOI: 10.1002/fld

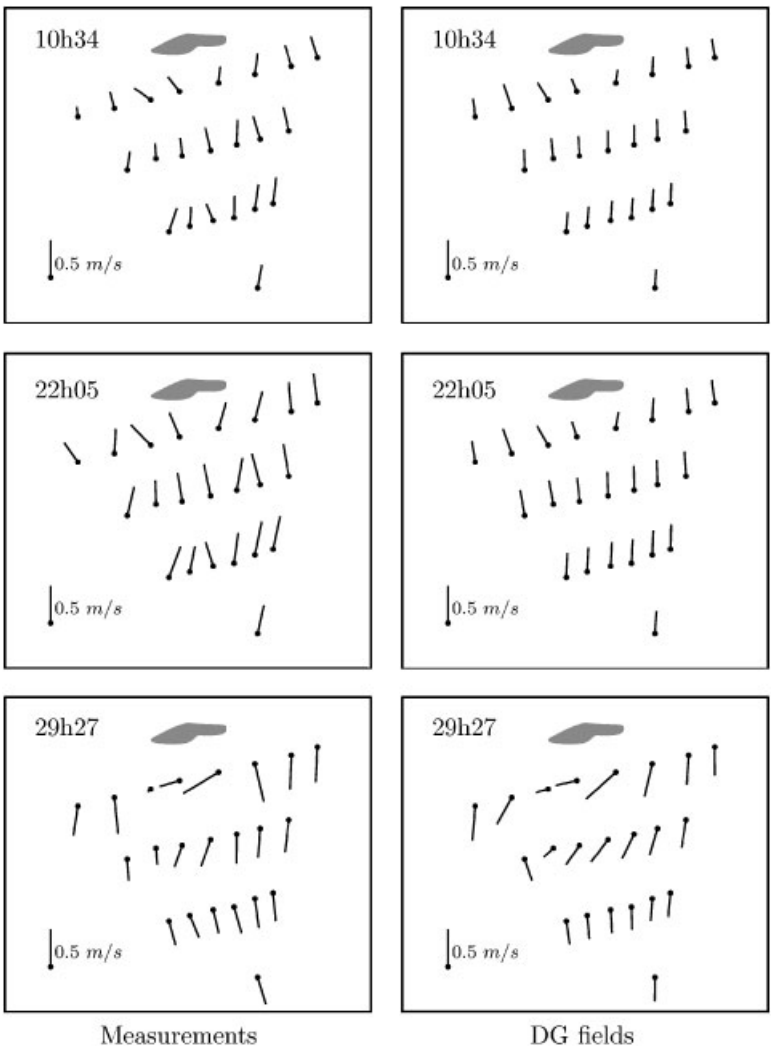

Figure 16. Comparison between the experimental data (left) and the DG results (right). The numerical results seem to fit the data with velocities of the right amplitudes and directions.

the currentmeters with a sufficiently high u-component is observed in Figure 14, i.e. in the eddy behind the island. Figures 16 and 17 depict the velocity fields measured in 1982 and the velocity field resulting from the DG computation at the same locations for several times. We observe that the numerical results are in good agreement with the measurement, considering the uncertainty on the bathymetry shape (measured on a $200\,\mathrm{m} \times 200\,\mathrm{m}$ grid), the island position, the currentmeters locations and considering the simplified tidal flow forcing assumed to propagate following a straight line parallel to the left and right boundaries of the domain. We obtain eddies of the same shapes and intensities and the velocity evolution seems to fit the data.

DOI: 10.1002/fld

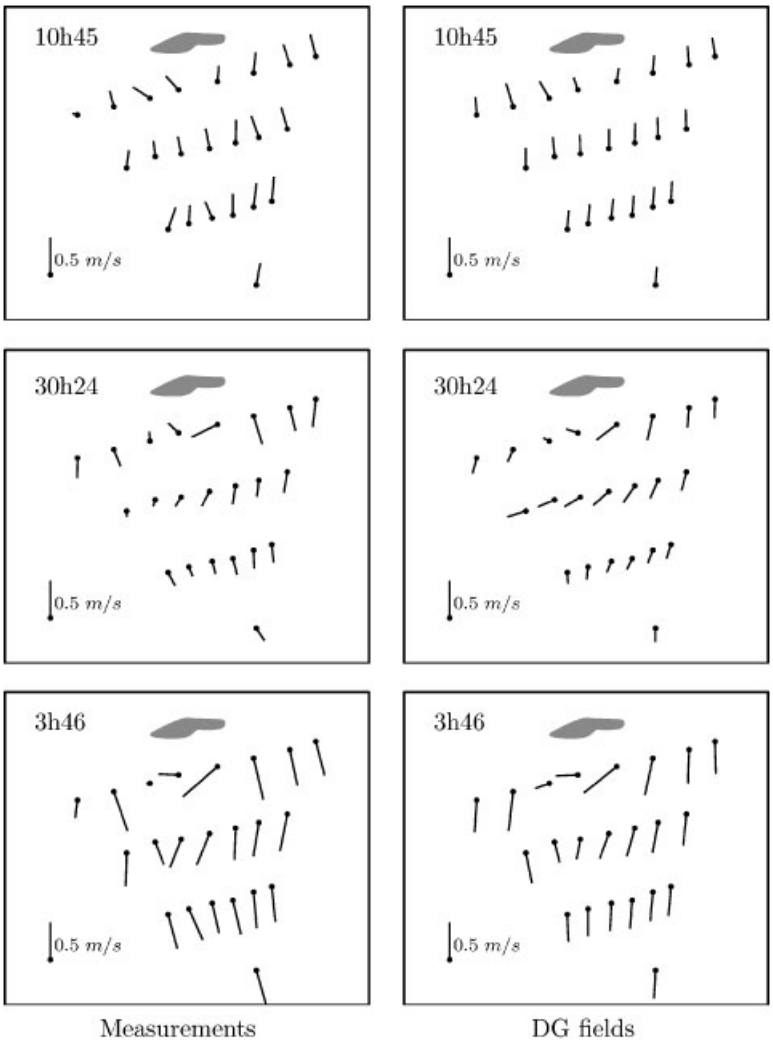

Figure 17. Comparison between the experimental data (left) and the DG results (right). The numerical results seem to fit the data with velocities of the right amplitudes and directions.

4. CONCLUSIONS

We have applied the DG method to the shallow water equations to solve a tidal flow around a shallow water island. Realistic parameters and data such as the tidal forcing, the bathymetry and the complex island shape were used. We have observed the importance of the boundary numerical representation in the context of ocean processes and especially quasi-steady tidal flows. Indeed, with the test case of a constant mean flow around a circle and a slip boundary condition, the shallow water equations present the same behaviour than the Euler equations: spurious oscillations appear on poor discretized boundaries, especially with the use of high-order function space,

DOI: 10.1002/fld

irregular coasts and quasi-steady flows. In the framework of an ocean model with thousands of coasts and islands, we cannot afford the same boundary discretization than for cylinder or airfoils studies. With very complex bluff bodies and very coarse meshes, some usually perfectly working techniques such as the smoothing of the normals may reveal inefficient to avoid oscillations and spurious eddies, while a second-order mapping still leads to very smooth solutions. Moreover, the continuous reconstruction of the normals on very coarse grids does not accurately represent the islands' shapes as the high-order curved meshes.

The Rattray test case highlights the fact that some non-physical eddies may have the right shapes and amplitudes for wrong reasons when using piecewise linear representations of the boundaries and high-order shape functions. Moreover, such a poor representation may lead to an unstable scheme for some specific data as a strong varying shallow bathymetry. The DG method with suitable boundary discretization provides an accurate model with a very low amount of diffusion so that no spurious eddy is created. A physical diffusive term may then be calibrated to accurately reproduce the subgrid-scale processes. The tidal flow around the Rattray island with the real configuration has then been compared with *in situ* measurements. The DG results are in very good agreement with the velocity data, considering the lack of accuracy on the tide direction, the island shape or the bathymetry.

Let us finally mention that the generation of curved meshes for high-order polynomial mappings is a critical issue in this framework, since the distortion of the elements has to be kept to a minimum to avoid large quadrature errors leading to spurious waves. Major improvements to the method could eventually be achieved by improving the mapping for high-order elements and by implementing p-adaptivity to reduce the computational costs for multi-scale computations in large domains.

Those preliminary results are quite promising and we believe that the DG method is a good candidate for the creation of an ocean model on unstructured grids. Much of work has still to be done as the extension of this bidimensional model to a 3D model or the extension to spherical geometries.

ACKNOWLEDGEMENTS

Paul-Emile Bernard is supported by the *Fonds pour la formation à la Recherche dans l'Industrie et dans l'Agriculture* (FRIA, Belgium). The present study was carried out within the scope of the project 'A second-generation model of the ocean system' funded by the *Communauté Française de Belgique*, as *Actions de Recherche Concertées*, under contract ARC 04/09-316. This study is a contribution to the SLIM[‡] project.

REFERENCES

1. Bryan K. A numerical method for the study of the circulation of the world ocean. *Journal of Computational Physics* 1969; **4**:347–376.
2. Fix GJ. Finite element models for ocean circulation problems. *SIAM Journal on Applied Mathematics* 1975; **29**:371–387.
3. Lynch DR, Ip JTC, Naimie CE, Werner FE. Comprehensive coastal circulation model with application to the gulf of maine. *Continental Shelf Research* 1996; **16**:875–906.

[‡]SLIM, Second-Generation Louvain-la-Neuve Ice-ocean Model, www.climate.be/SLIM.

DOI: 10.1002/fld

4. Pain CC, Piggott MD, Goddard AJH, Fang F, Gorman GJ, Marshall DP, Eaton MD, Power PW, de Oliveira CRE. Three-dimensional unstructured mesh ocean modelling. *Ocean Modelling* 2004; **10**:5–33.
5. Pietrzak J, Deleersnijder E, Schröter J. The second international workshop on unstructured mesh numerical modelling of coastal, shelf and ocean flows. *Ocean Modelling* 2005; **10**:1–252 (Special Issue).
6. White L, Deleersnijder E. Diagnoses of vertical transport in a three-dimensional finite-element model of the tidal circulation around an island. *Estuarine, Coastal and Shelf Science* 2007; **74**:655–669.
7. Casulli V, Walters RA. An unstructured grid, three-dimensional model based on the shallow-water equations. *International Journal for Numerical Methods in Fluids* 2000; **32**(3):331–346.
8. Ham DA, Pietrzak J, Stelling GS. A scalable unstructured grid 3-dimensional finite volume model for the shallow water equations. *Ocean Modelling* 2005; **10**:153–169.
9. Iskandarani M, Haidvogel DB, Levin JC. A three-dimensional spectral element model for the solution of the hydrostatic primitive equations. *Journal of Computational Physics* 2003; **186**:397–425.
10. Cockburn B, Karniadakis GE, Shu C-W. *Discontinuous Galerkin Methods*. Lecture Notes in Computational Science and Engineering. Springer: Berlin, 2000.
11. Chevaugeon N, Hillewaert K, Gallez X, Ploumhans P, Remacle J-F. Optimal numerical parameterization of discontinuous Galerkin method applied to wave propagation problems. *Journal of Computational Physics* 2007; **223**:188–207.
12. Chevaugeon N, Remacle J-F, Gallez X, Ploumans P, Caro S. Efficient discontinuous Galerkin methods for solving acoustic problems. *Eleventh AIAA/CEAS Aeroacoustics Conference*, Monterey, CA, 23–25 May 2005.
13. Warburton T, Karniadakis GE. A discontinuous Galerkin method for the viscous mhd equations. *Journal of Computational Physics* 1999; **152**:608–641.
14. Remacle J-F, Li X, Shephard MS, Flaherty JE. Anisotropic adaptive simulation of transient flows using discontinuous Galerkin methods. *International Journal for Numerical Methods in Engineering* 2005; **62**(7): 899–923.
15. Nair RD, Thomas SJ, Loft RD. A discontinuous Galerkin global shallow water model. *Monthly Weather Review* 2005; **133**:876–888.
16. Giraldo FX, Hesthaven JS, Warburton T. Nodal high-order discontinuous Galerkin methods for the spherical shallow water equations. *Journal of Computational Physics* 2002; **181**:499–525.
17. Dawson C, Proft J. Coupled discontinuous and continuous Galerkin finite element methods for the depth-integrated shallow water equations. *Computer Methods in Applied Mechanics and Engineering* 2004; **193**(3–5):289–318.
18. Adjerid S, Devine KD, Flaherty JE, Krivodonova L. A posteriori error estimation for discontinuous Galerkin solutions of hyperbolic problems. *Computer Methods in Applied Mechanics and Engineering* 2002; **191**: 1097–1112.
19. Bernard P-E, Chevaugeon N, Legat V, Deleersnijder E, Remacle J-F. High-order *h*-adaptive discontinuous Galerkin methods for ocean modeling. *Ocean Dynamics* 2007; **57**:109–121.
20. Ainsworth M. Dispersive and dissipative behavior of high order discontinuous Galerkin finite element methods. *Journal of Computational Physics* 2004; **198**(1):106–130.
21. Hu F, Atkins H. Eigensolution analysis of the discontinuous Galerkin method with nonuniform grids *i* one space dimension. *Journal of Computational Physics* 2002; **182**(2):516–545.
22. Bernard P-E, Remacle J-F, Legat V. Dispersion analysis of discontinuous Galerkin schemes applied to Poincaré, Kelvin and Rossby waves. *Journal of Scientific Computing* 2008; **34**:26–47.
23. Bassi F, Rebay S. A high-order accurate discontinuous finite element solution of the 2d Euler equations. *Journal of Computational Physics* 1997; **138**:251–285.
24. Krivodonova L, Berger M. High order accurate implementation of solid wall boundary conditions in curved geometries. *Journal of Computational Physics* 2006; **211**:492–512.
25. Lambrechts J, Hanert E, Deleersnijder E, Bernard P-E, Legat V, Remacle J-F, Wolanski E. A multiscale model of the whole great barrier reef hydrodynamics. *Estuarine, Coastal and Shelf Science* 2008; DOI: 10.1016/j.ecss.2008.03.016.
26. Wolanski E. *Physical Oceanographic Processes of the Great Barrier Reef*. CRC Press: Boca Raton, FL, 1994.
27. Wolanski E, Asaeda T, Tanaka T, Deleersnijder E. Three-dimensional island wakes in the field, laboratory and numerical codes. *Continental Shelf Research* 1996; **16**:1437–1452.
28. Godunov SK. Finite difference methods for the computation of discontinuous solutions of the equations of fluid dynamics. *Matematicheskii Sbornik* 1959; **47**:271–306.
29. Roe PL. Approximate Riemann solvers, parameter vectors and difference schemes. *Journal of Computational Physics* 1981; **43**:357–372.

30. Toro EF. *Riemann Solvers and Numerical Methods for Fluid Dynamics*: *A Practical Introduction*. Springer: Berlin, 1997.
31. LeVeque RJ. *Finite Volume Methods for Hyperbolic Problems*. Cambridge Texts in Applied Mathematics. Cambridge University Press: Cambridge, 2002.
32. Remacle J-F, Soares Frazão S, Li X, Shephard MS. An adaptive discretization of shallow-water equations based on discontinuous Galerkin methods. *International Journal for Numerical Methods in Fluids* 2006; **52**:903–923.
33. Arnold DN, Brezzi F, Cockburn B, Marini LD. Unified analysis of discontinuous Galerkin methods for elliptic problems. *SIAM Journal on Numerical Analysis* 2002; **39**:1749–1779.
34. Bassi F, Rebay S. A high-order accurate discontinuous finite element method for the numerical solution of the compressible Navier–Stokes equations. *Journal of Computational Physics* 1997; **131**:267–279.
35. Cockburn B, Shu CW. The local discontinuous Galerkin finite element method for convection–diffusion systems. *SIAM Journal on Numerical Analysis* 1998; **35**:2440–2463.
36. Douglas J, Dupont T. *Interior Penalty Procedures for Elliptic and Parabolic Galerkin Methods*. Lecture Notes in Physics. Springer: Berlin, 1976.
37. Riviere B, Wheeler MF, Girault V. Improved energy estimates for interior penalty, constrained and discontinuous Galerkin methods for elliptic problems *i*. *Computational Geosciences* 1999; **3**:337–360.
38. Pedlosky J. *Geophysical Fluid Dynamics*. Springer: Heidelberg, 1979.
39. Cushman-Roisin B. *Introduction to Geophysical Fluid Dynamics*. Prentice-Hall: New York, 1994. ISBN: 0-13-353301-8.
40. Shephard MS, Flaherty JE, Jansen KE, Li X, Luo X, Chevaugeon N, Remacle J-F, Beall MW, O'Bara RM. Adaptive mesh generation for curved domains. *Applied Numerical Mathematics* 2005; **52**:251–271.
41. Geuzaine C, Remacle J-F. Gmsh: a three-dimensional finite element mesh generator with built-in pre- and post-processing facilities. *International Journal for Numerical Methods in Engineering* 2008; submitted.
42. Wolanski E, Imberger J, Heron ML. Island wakes in shallow coastal waters. *Journal of Geophysical Research* 1984; **89**(C14):10553–10569.
43. Smagorinsky J. General circulation experiments with the primitive equations: 1. The basic experiment. *Monthly Weather Review* 1963; **91**(5):99–165.
44. Falconer RA, Wolanski E, Mardapitta-Hadjipandeli L. Modeling tidal circulation in an island's wake. *Journal of Waterway*, *Port*, *Coastal and Ocean Engineering* 1986; **112**(2):234–254.
45. Deleersnijder E, Norro A, Wolanski E. A three-dimensional model of the water circulation around an island in shallow water. *Continental Shelf Research* 1992; **12**:891–906.

DOI: 10.1002/fld